1 # Modelling of street-scale pollutant dispersion by coupled simulation of
2 chemical reaction, aerosol dynamics, and CFD

3 Chao Lin [a,*,★], Yunyi Wang [b,★], Ryozo Ooka [c], Cédric Flageul [d], Youngseob Kim [b],
4 Hideki Kikumoto [c], Zhizhao Wang [b], Karine Sartelet [b]
5 [a] Graduate School of Engineering, The University of Tokyo, 4-6-1 Komaba, Meguro-ku,
6 Tokyo 153-8505, Japan
7 [b] CEREA, École des Ponts ParisTech, EdF R&D, 77 455 Marne la Vallée, France
8 [c] Institute of Industrial Science, The University of Tokyo, 4-6-1 Komaba, Meguro-ku,
9 Tokyo 153-8505, Japan
10 [d] Curiosity Group, Pprime Institute, Université de Poitiers, CNRS, ISAE-ENSMA,
11 Chasseneuil, France
12 [*] Corresponding author, c-lin415@iis.u-tokyo.ac.jp
13 ★These authors contributed equally to this work.

15 ABSTRACT

16 In the urban environment, gas and particles impose adverse impacts on pedestrians' health.
17 The conventional computational fluid dynamics (CFD) methods that regard pollutant as
18 passive scalar cannot reproduce the formation of secondary pollutants and lead to
19 uncertain prediction. In this study, SSH-Aerosol, a modular box model that simulates the
20 evolution of gas, primary and secondary aerosols, is coupled with the CFD softwares
21 OpenFOAM and Code_Saturne. The transient dispersion of pollutants emitted from
22 traffic in a street canyon is simulated using unsteady Reynolds-averaged Navier–Stokes
23 equations (RANS) model. The simulated concentrations of NO_2, PM_{10} and black carbon
24 are compared with field measurements on a street of Greater Paris. The simulated NO_2
25 and PM_{10} concentrations based on the coupled model achieved better agreement with
26 measurement data than the conventional CFD simulation. Meanwhile, the black carbon
27 concentration is underestimated, probably partly because of the underestimation of non-
28 exhaust emissions (tyre and road wear). Aerosol dynamics lead to large increase of
29 ammonium nitrate and anthropogenic organic compounds from precursor-gas emitted in
30 the street canyon.

32 Keywords
33 Pollutant dispersion, Street canyon, Aerosol dynamics, CFD, PM_{10}, Secondary aerosols

35 **1. Introduction**
36 Traffic-related pollutants can impose adverse effects on pedestrians' health in the urban

environment (Anenberg et al., 2017; Jones et al., 2008). Especially, particulate matter (PM) is strongly associated with increased cardiovascular diseases (Du et al., 2016). Therefore, investigating the dispersion of PM and the corresponding precursor gas is of great significance to evaluate the environmental impact and devise suitable countermeasures (Kumar et al., 2008).

With the development of numerical simulations, computational fluid dynamics (CFD) has been widely used for near-field dispersion prediction (Tominaga and Stathopoulos, 2013). The pollutant dispersion patterns in complex geometric and non-uniform building configurations can be well predicted using CFD simulations (Blocken et al., 2013). Pollutant dispersion, deposition and transformation (chemical reactions and aerosol dynamics) have primary roles in near-field prediction models. However, most CFD-based studies assume that the time scale of transport at the street scale (~ 100 m) is relatively shorter than the time scale of deposition and transformation; therefore, they frequently regard pollutants as inert matter. Meanwhile, the recirculation flows which commonly exist in street canyons lead to low-ventilation zones and may provide sufficient time for transformation (Lo and Ngan, 2017; Zhang et al., 2020).

In addition, when PM is transported as a passive scalar, the distribution of the total concentration can be simulated, however, information on the particle size distribution and chemical composition is unclear. Understanding the size distribution is important for evaluating the health hazards because large particles are deposited in the mouth and upper airways, whereas smaller particles deposit deeper in the lungs and can even reach the alveolar region of the lungs (Sung et al., 2007). In addition, as particles of different chemical compositions are related to different sources and/or precursor gases, gaining knowledge of their composition may help devise countermeasures to limit their concentrations (Kim, 2019).

To simulate pollutant concentrations considering both transport and transformation, many studies have coupled air-quality models with gas-phase chemistry and aerosol modules and achieved chemical transport from a regional scale (~100 km) (Sartelet et al., 2007) to a street scale (Lugon et al., 2021b). However, few models can simultaneously represent detailed particle dispersion in a complicated urban flow field considering secondary aerosol formation.

For the recent development and application of CFD-chemistry coupling model, Kurppa et al., (2019) implemented a sectional aerosol module into large eddy simulation (LES), and conducted a particle dispersion simulation on a neighborhood scale. Gao et al., (2022) employed the same model to examine the dispersion of cooking-generated aerosols in an urban street canyon. In both studies, the effect of particle dynamics on aerosol number

73 concentration was well reproduced. However, the simulated chemical composition was
74 not detailed. In addition, the chemical reactions of the precursor gas were not considered.
75 Kim et al., (2019) coupled unsteady Reynolds-averaged Navier-Stokes (RANS) model
76 with gas chemistry and aerosol modules and conducted simulations of PM_1 in a street
77 canyon under summer and winter conditions. The diurnal variations, spatial distribution
78 and chemical composition of pollutants in the street canyon were investigated. However,
79 the size distribution of particles and the secondary organic aerosol (SOA) chemistry were
80 not considered. Therefore, a more comprehensive coupled model is needed to simulate
81 the evolution of gas concentrations, mass and number concentrations of primary and
82 secondary particles at the same time.

83 Vehicles are considered to be the main ammonia (NH_3) source in urban environments
84 (Sun et al., 2017). Reactive nitrogen emissions from many new vehicles are now
85 dominated by NH_3 (Bishop and Stedman, 2015). Since the formation of ammonium
86 nitrate is often limited by HNO_3 rather than NH_3 in urban areas (NH_3-limited), increasing
87 NH_3 may lead to increased ammonium nitrate production and PM concentration in urban
88 streets (Lugon et al., 2021b). However, NH_3 emissions from passenger cars are usually
89 not regulated (Suarez-Bertoa and Astorga, 2018). Therefore, to provide evidence in
90 making policies for NH_3 emission regulation, it is important to investigate the local
91 influence of NH_3 emissions on PM concentrations.

92 Therefore, to achieve a more comprehensive simulation of PM and related precursor gas,
93 this study couple two open-source CFD softwares: OpenFOAM (OpenFOAM user guide)
94 and Code_Saturne (Archambeau et al., 2004), with gas-phase chemistry and aerosol
95 module SSH-Aerosol (Sartelet et al., 2020). Both OpenFOAM and Code_Saturne own
96 wide users. Therefore, coupling SSH-aerosol with both CFD softwares may satisfy more
97 needs. Simulations of the PM concentrations in a two-dimensional street canyon are
98 conducted. The coupled model is validated by comparison to field measurements. The
99 size distributions and chemical compositions of particles from the models with and
100 without secondary aerosol formation are compared. In addition, cases with large NH_3
101 emissions are considered and the related PM increase is investigated.

102 The remainder of this paper is organized as follows. The coupling of the aerosol model
103 and CFD is introduced in Section 2. The computational details are presented in Section 3.
104 In Section 4, the simulated pollutant concentrations are compared with field
105 measurements, followed by evaluations of the influence of the grid, coupling method and
106 time step. In Section 5, spatial and temporal variations in the concentrations are analyzed.
107 The chemical compositions and size distributions of the particles between the coupled
108 model and the model that does not consider gas chemistry or aerosol dynamics are

109 compared. In addition, the effect of NH_3 traffic emissions on particle concentrations is
110 discussed. Finally, the conclusions and perspectives are presented in Section 6.
111
112 **2. Model description**
113 The coupling method between CFD and chemistry modules is similar to the literature
114 (Gao et al., 2022; Kurppa et al., 2019). OpenFOAM v2012 and Code_Saturne 6.2 are
115 used to solve the governing equations of the flow field and transport equations of gas and
116 particle mass fractions. The inflow conditions, pollutants' background concentrations and
117 emission rates are obtained from regional models, and are linearly interpolated into each
118 time step, which will be introduced in Section 3. This simulation method is called
119 transient-condition method (TCM) in this study. However, because time-varying flow
120 fields and concentration fields are expensive to compute in terms of computational time,
121 conducting CFD simulations with fixed boundary conditions and emission rates at
122 specific time points is considered a practical method for evaluating street-level pollutant
123 concentrations (Wu et al., 2021; Zhang et al., 2020). The transport (advection and
124 diffusion) and chemical processes will reach equilibrium, and the simulated
125 concentrations will reach quasi-stable values. These values are often regarded as time-
126 averaged concentrations. This method is called the constant-condition method (CCM) in
127 this study, in contrast to TCM. However, the simulation accuracy of CCM has not been
128 validated in simulations that consider both gas chemistry and particle dynamics.
129 Therefore, validation is conducted using boundary conditions and emission rates at
130 specific time points and the simulated concentrations with CCM and TCM are compared
131 in Section 4.2.
132 The unsteady RANS model is used for the transient simulations with both CFD codes. In
133 OpenFOAM, the RNG (Re-Normalisation Group) k–ε model (Yakhot et al., 1992) is
134 deployed for turbulence closure. All transport equations are discretized using the total
135 variation diminishing (TVD) scheme (Harten, 1984; Yee, 1987), which combines the
136 first-order upwind difference scheme and the second-order central difference scheme. The
137 PIMPLE algorithm, a merged PISO (Pressure Implicit with Splitting of Operator)–
138 SIMPLE (Semi-Implicit Method for Pressure-Linked Equations) algorithm in the
139 OpenFOAM toolkit, is used for pressure–velocity coupling. In Code_Saturne, turbulence
140 is solved using the k–ε turbulence model (linear production) (Guimet and Laurence, 2002).
141 The time and space discretizations of velocity, pressure and other scalars in all transport
142 equations are realized through a centred scheme and a fractional step scheme
143 (Archambeau et al., 2004) . For both CFD software, the dry deposition schemes for gas
144 and particle are added to the transport equations using volume sink terms based on Zhang

145 et al. (2003) and Zhang et al. (2001), respectively. The details of the implementation are
146 provided in Appendix A.
147 SSH-Aerosol (Sartelet et al., 2020) is a modular box model that simulates the evolution
148 of not only gas concentrations but also the mass and number concentrations of primary
149 and secondary particles. In SSH-Aerosol 112 gas species and 40 particle species are
150 considered. The particle compounds are dust, black carbon, inorganics (sodium, sulphate,
151 ammonium, nitrate and chloride), primary organic aerosol (POA) and secondary organic
152 aerosol (SOA). Three main processes involved in aerosol dynamics (coagulation,
153 condensation /evaporation and nucleation) are included. The particle size distribution is
154 modelled using a sectional size distribution. Nucleation is not considered in this study
155 because only the mass and not the number of particles is available for evaluation, and
156 large uncertainties remain on the nucleation parameterizations (Sartelet et al., 2022)
157 mostly affecting the number of particles. As nucleation is not considered, the minimum
158 diameter does not need to be as low as 0.001 μm, and it is fixed to 0.01 μm, as in the
159 regional-scale simulations of Sartelet et al. (2018), which provide the background
160 concentrations. Six particle size sections are employed with bound diameters of 0.01, 0.04,
161 0.16, 0.4, 1.0, 2.5 and 10 μm.
162 The coupling between CFD and SSH-aerosol are achieved by using the application
163 program interface (API) of SSH-aerosol. The gas and particle concentrations are
164 initialized in CFD and are transported in the domain for each time step. For each grid
165 volume cell, these transported concentrations, as well as meteorological parameters, such
166 as temperature and humidity, are then sent to SSH-aerosol to advance one time step of
167 gaseous chemistry and aerosol dynamics. Once the SSH-aerosol calculation is completed,
168 the concentrations are sent back to the CFD for the next time step. It should be noted that
169 as the SSH-aerosol processes the ensemble-averaged concentration from RANS model,
170 the covariance of turbulent diffusion and chemical reaction may not be fully reproduced.
171 The influence of different operator splitting algorithms is discussed in Section 4.4.
172

173   **3. Simulation setup**
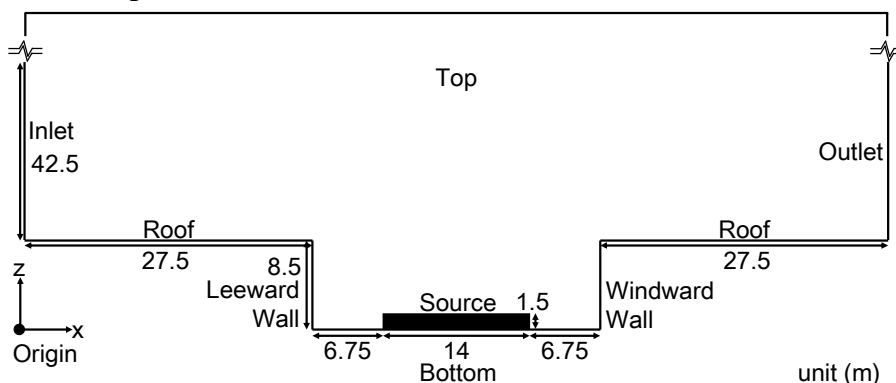
174
175   Fig. 1 Simulation domain of street canyon

176

177   The simulation is set up to model a street in Greater Paris (Boulevard Alsace-Lorraine),
178   where field measurements were conducted from April 6 to June 15, 2014. The
179   concentrations of nitrogen dioxide (NO_2), particles with diameters less than 10 µm (PM_{10}),
180   and black carbon were measured as described in (Kim et al., 2018). Fig. 1 shows the
181   simulation domain. The 2-D street canyon is 27.5 m in width (W) and 8.5 m in height
182   (H). The domain height is 6 H. The street canyon is discretized into uniform grids in x-
183   and z- directions. The grid resolutions in the street canyon are 0.5 m in both x-and z-
184   directions, respectively. The largest grid sizes are 4 m (x) × 2m (z). An analysis of the
185   grid sensitivity is described in Section 4.3.
186   Simulations are conducted from 4:30 a.m. to 5 p.m. on April 30, 2014 at local time
187   (GMT+2). This period is selected because the wind direction is almost perpendicular to
188   the street canyon during that day, allowing for a 2D simulation setting. During the field
189   measurement, there exists several time periods that the wind direction is perpendicular
190   with the street canyon. Meanwhile, some time periods are short (less than 5 hours), and
191   we consider that short period simulation is not representative in simulation accuracy. In
192   addition, we consider that it is critical to have a simulation time long enough to cover
193   both day-time chemistry and night-time chemistry. The first 30 minutes of the simulation
194   corresponds to model spin-up, and the simulation lasts 12 hours. A sensitivity analysis of
195   numerical aspects, such as the splitting method between transport and chemistry and the
196   time step, is described in Section 4.4.
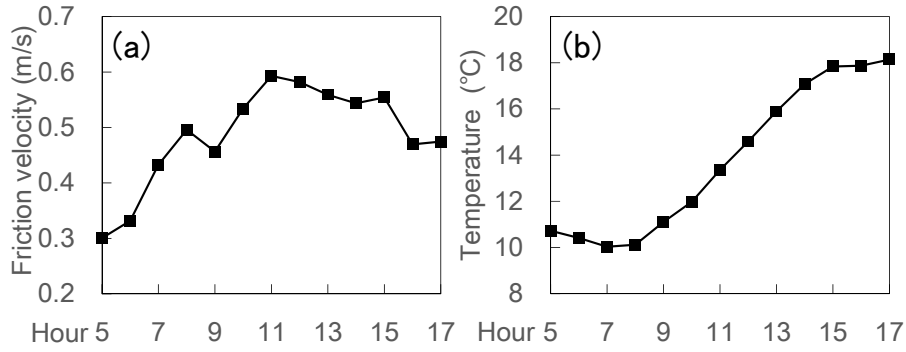
Fig. 2 Time variations of hourly friction velocity and temperature for inflow.

Meteorological conditions (Fig. 2) including time-varying friction velocity and temperature are obtained from the simulation described in Sartelet et al. (2018) using the Weather Research and Forecasting (WRF) model. The grid resolution is 1 km ×1 km in Paris. The lowest and highest friction velocities occurred approximately at 5 a.m. and 11 a.m., respectively. The lowest and highest temperatures are around 8 a.m. and 5 p.m. For the inflow, the wind direction is perpendicular to the street canyon. The friction velocity u_* is used to prescribe the vertical profiles of the streamwise velocity U, turbulent kinetic energy k and turbulent dissipation rate ε as follows

$$U(z) = \frac{u_*}{\kappa} \ln\left(\frac{z - H}{z_0}\right) \tag{1}$$

$$k(z) = \frac{u_*^2}{\sqrt{C_\mu}} \tag{2}$$

$$\varepsilon(z) = \frac{u_*^3}{\kappa(z - H)} \tag{3}$$

where κ is the von Kármán constant and C_μ is the model constant (=0.09) in the k-ε model. The roughness length z_0 is set to 1 m for the inlet (Belcher, 2005) and 0.1 m for the wall and bottom (Lo and Ngan, 2015).

In addition, since the domain height is low (51 m) in this study and we focus on the pollutant dispersion behaviors in the street canyon, it is reasonable to consider the atmospheric stability as neutral; therefore the temperature is assumed to be spatially uniform at the inflow. The hourly friction velocities and temperatures are linearly interpolated into each timestep and prescribed at the inflow.
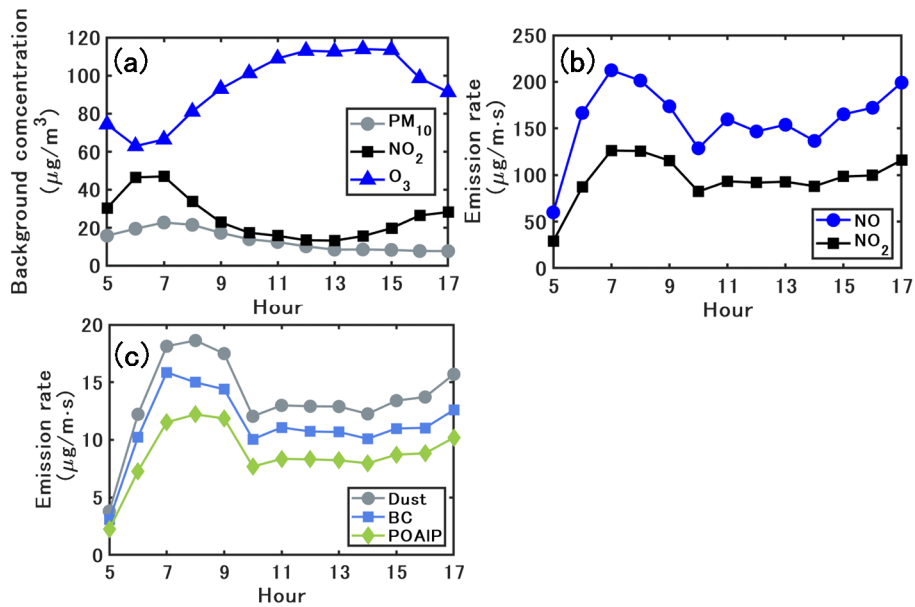
Fig. 3 Time variations of (a) PM_{10}, NO and NO_2 background concentrations, (b) emission rates of NO and NO_2 and (c) emission rates of dust, BC and organics (POAlP).

Fig. 3(a) shows the time variations of the PM_{10}, NO and NO_2 background concentrations. Fig. 3(b) and (c) show the emission rates for NO, NO_2 and the emitted compounds of PM_{10}. The background concentrations of the gas and particles are obtained from the regional-scale simulations of Sartelet et al. (2018) with the Eulerian model Polair3D of the Polyphemus air quality modelling platform (Mallet et al., 2007), which uses the same chemical representation as in this study. As detailed in Sartelet et al. (2018), the regional background concentrations compare well to measurements of O_3, NO_2, PM_{10}, $PM_{2.5}$, black carbon and organic aerosols. The hourly background concentrations are linearly interpolated into each timestep and prescribed at the inflow and top. The traffic emission source is assumed to be approximately 14 m in width and 1.5 m in height, and it is set in the middle of the bottom of the canyon (Fig. 1). As detailed in Kim et al. (2022), emissions are estimated from the fleet composition and the number of vehicles in the street using COPERT's emission factors (COmputer Program to calculate Emissions from Road Transport, version 2019, EMEP/EEA, 2019). After the speciation of NO_x, Volatile Organic Compounds (VOC), $PM_{2.5}$ and PM_{10} into model species, emissions are set for 16 gaseous model species and three particle model species: dust and unspecified matter (Dust), black carbon (BC) and primary organic aerosol of low volatility (POAlP). The PM size distribution at emission is assumed to be the same as in the previous studies (Lugon et al., 2021a, 2021b). The exhaust primary PM is assumed to be in the size bin [0.04 – 0.16 μm] while non-exhaust primary PM is coarser in the size bin [0.4 – 10 μm].

241 For the boundary conditions of the OpenFOAM, the pressure and the gradients of all other
242 variables are set to zero at the outlet. For the walls, we use the wall functions of ε and
243 turbulent kinematic viscosity ν_t for atmospheric boundary layer modelling in
244 OpenFOAM toolkit (OpenFOAM user guide) based on (Parente et al., 2011). The
245 gradients of turbulent kinetic energy k, concentration, and temperature are set to zero. In
246 Code_Saturne, a two-scales logarithmic friction velocity wall function is used for solving
247 the fluid velocity near wall cell and a three layers wall function is used for computing
248 other transported scalar profiles such as temperature near the wall (Arpaci and Larsen,
249 1984).
250 The turbulent Schmidt number Sc_t in the concentration transport equations, which is the
251 ratio of the turbulent diffusivity to the concentration and turbulent kinematic viscosity, is
252 important in turbulent diffusion modeling. The value of Sc_t is considered between 0.2
253 and 1.3, depending on the flow properties and geometries (Tominaga and Stathopoulos,
254 2007). For urban environments with a compact layout, a small $Sc_t = 0.4$ is found to
255 show better agreement with wind tunnel experiment data (Di Sabatino et al., 2007).
256 Therefore, a value of 0.4 is adopted in the current study.
257

258 4. Model evaluation

259 *4.1. Validation with field measurements and comparison of simulated concentrations with*
260 *the two CFD software*
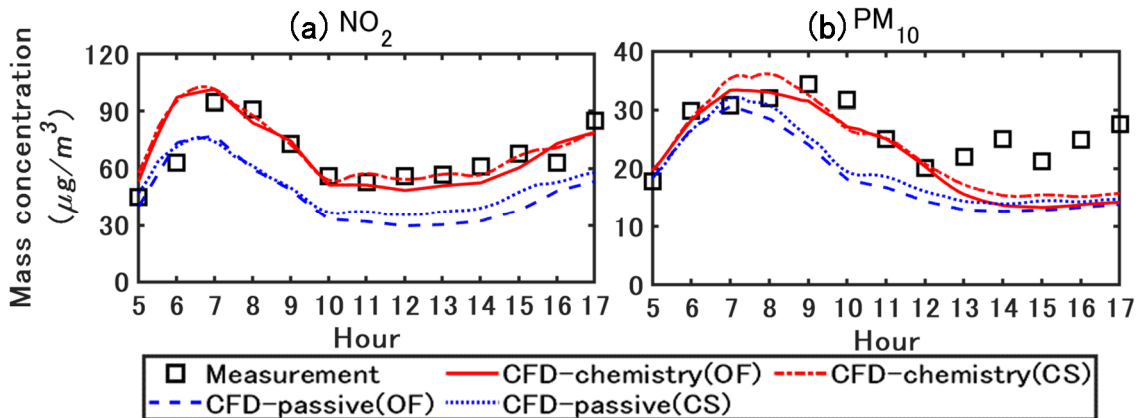
261
262 Fig. 4 Measured and simulated NO_2 and PM_{10} concentrations. The values are spatially
263 averaged in the street canyon ($27.5 \leq x \leq 55, 0 \leq z \leq 8.5$ m). CFD-passive and CFD-
264 chemistry denote the CFD simulation without and with chemistry coupling. OF and CS
265 denote the simulated concentrations based on OpenFOAM and Code_Saturne. All
266 concentrations are represented in local time (GMT+2).
267
268 Reproducing the flow field is important in this study. Meanwhile, the observation data on

269   wind velocity is not available. Therefore, we conducted a velocity validation for
270   OpenFOAM v2012 using data from a wind tunnel experiment (Blackman et al., 2015).
271   The predicted mean velocity agreed well with the experimental values. The details can be
272   found at Appendix B.

273   Fig. 4 compares the simulated concentrations with those obtained from the field
274   measurements. In the field measurements, the measured concentration was obtained from
275   averaging over two measurement points near the leeward and windward walls in the street
276   canyon. In this section, the simulated results and discussion are based on the spatially-
277   averaged values in the street canyon ($27.5 \leq x \leq 55, 0 \leq z \leq 8.5$ m). CFD-passive and
278   CFD-chemistry denote the CFD simulation without and with chemistry coupling. OF and
279   CS denote simulated concentrations based on OpenFOAM and Code_Saturne. The
280   operator splitting order and time step for OF and CS are the A-B-A splitting method with
281   0.5 s and the A-B splitting method with 0.25 s, as detailed in Section 4.4. The simulation
282   time ratio of CFD-chemistry and CFD-passive is about three times in both OpenFOAM
283   and Code_Saturne in this study.

284   For NO_2, the peak concentration in the field measurement occurred approximately at 7
285   a.m. owing to the morning traffic. In the CFD-passive simulations, the lack of chemical
286   reactions lead to an underestimation of NO_2, while the concentrations simulated with
287   CFD-chemistry agree well with the measurements. For PM_{10}, the concentrations
288   simulated with CFD-chemistry also show better agreement with the measurements than
289   CFD-passive. The primary reason is that CFD-chemistry can reproduce the condensation
290   of inorganic and organic matter from the gas phase to the particle phase, which will be
291   further explained in the following sections. The simulation results based on OF and CS
292   show small differences, and detailed comparisons are presented in Fig. 6.

293   Validation metrics (Chang and Hanna, 2004) are used to quantify the overall accuracy of
294   the CFD simulated concentrations based on OF, compared with the measured values
295   (Trini Castelli et al., 2018; Ferrero et al., 2019). The following metrics are used: fractional
296   bias (FB), geometric mean bias (MG) and normalized mean square error (NMSE). These
297   metrics are defined as follows:

$$\text{FB} = \frac{\overline{Obs} - \overline{CFD}}{0.5(\overline{Obs} + \overline{CFD})} \tag{4}$$

$$\text{MG} = \exp(\overline{\ln Obs} - \overline{\ln CFD}) \tag{5}$$

$$\text{NMSE} = \frac{\overline{(Obs_i - CFD_i)^2}}{\overline{Obs} \times \overline{CFD}} \tag{6}$$

298   where Obs_i and CFD_i are the measured and CFD simulated concentrations for the
299   compound/species i, respectively. The overbar represents the mean value of the entire

dataset. The ideal values are 1 for MG, and 0 for FB and NMSE. Previous research has suggested that $|FB| < 0.3$, $0.7 < MG < 1.3$ and $NMSE < 4$ are acceptable for simulated concentrations (Hanna et al., 2004).

Table 1 shows the statistical indicators for spatially averaged concentrations of NO_2 and PM_{10} in the street canyon from 5 a.m. to 5 p.m. For NO_2 and PM_{10}, the mean and 90% percentile concentrations simulated with CFD-chemistry are closer to the measurements than those simulated with CFD-passive. In addition, the FB, MG and NMSE values of CFD-chemistry are closer to the ideal values than those of CFD-passive.

Table 1 Statistical indicators for NO_2 and PM_{10} in the street canyon from 5 a.m. to 5p.m. The concentrations are simulated with OpenFOAM.

	Concentration ($\mu g/m^3$)		Validation metrics		
NO_2	Mean	Percentile 90%	FB	MG	NMSE
Measurement	66.6	91.8	/	/	/
CFD-chemistry	67.3	97.3	-0.01	1.00	1E-4
CFD-passive	45.9	73.7	0.36	1.50	0.14
PM_{10}	Mean	Percentile 90%	FB	MG	NMSE
Measurement	26.4	32.5	/	/	/
CFD-chemistry	22.3	33.1	0.17	1.23	0.03
CFD-passive	18.8	28.9	0.34	1.45	0.13
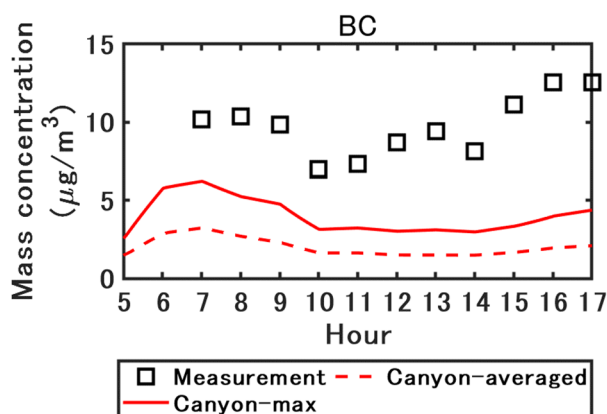
Fig. 5 Measured and simulated black carbon concentrations with OpenFOAM. The canyon-averaged and maximum concentrations in the street canyon are represented by the plain line and the dashed line respectively ($27.5 \leq x \leq 55, 0 \leq z \leq 8.5$ m).

The black carbon (BC) concentration simulated with OF is compared with the

318   measurements in Fig. 5. Because BC is considered an inert matter, considering chemistry
319   does not influence the mass concentration. Therefore, the concentrations simulated with
320   CFD-passive and CFD-chemistry show little difference; only the concentration simulated
321   with CFD-chemistry is shown here. The BC concentrations are underestimated by a factor
322   of approximately 5. Even the maximum concentrations in the street canyon largely
323   underestimate the measurements. One of the causes of this underestimation may be the
324   underestimation of the non-exhaust tyre emission factors in the COPERT emission factors
325   used here (Lugon et al., 2021a).
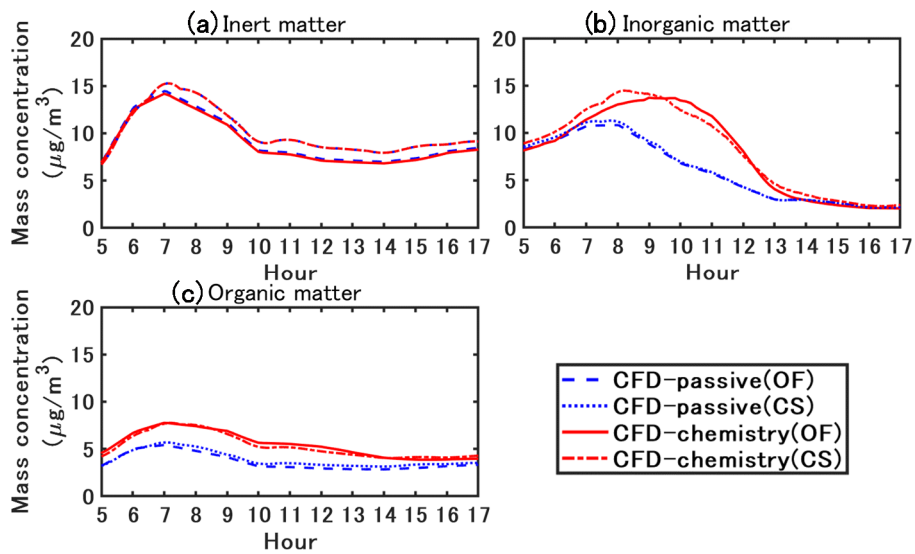
326
327   Fig. 6 Simulated particle concentrations with OpenFOAM (OF) and Code_Saturne (CS).
328   CFD-passive and CFD-chemistry denote the CFD simulation without and with chemistry
329   coupling.
330
331   The particle concentrations simulated with OF and CS are compared in Fig. 6. The
332   evolutions of the concentrations simulated by OF and CS are similar. Higher PM_{10}
333   concentrations are simulated by CS around 8 a.m. during the traffic peak and in the
334   afternoon, mostly because of the higher concentrations of emitted inert compounds, such
335   as black carbon and dust. Differences in the turbulence scheme may explain these
336   variations. Meanwhile, the difference between CFD-passive and CFD-chemistry for the
337   inorganic and organic matter is in accordance with OF and CS, showing the robustness
338   of the coupling method between CFD and SSH-aerosol by API. For simplicity, only the
339   simulated concentration based on OF is presented and discussed in the following sections.
340

341   *4.2. Transient-condition method and constant-condition method*
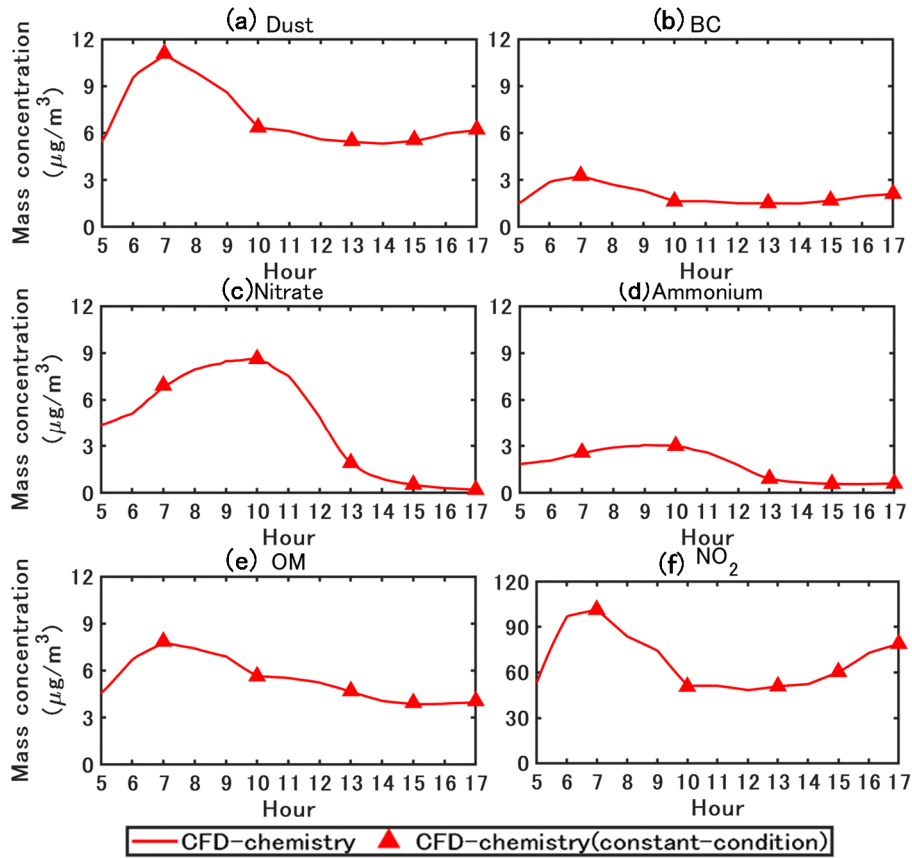
342
343   Fig. 7 Simulated PM$_{10}$ and NO$_2$ concentrations with the transient-condition and constant-
344   condition methods. The concentrations are spatially averaged in the street canyon.
345
346   To validate the simulation accuracy of CCM in simulations that consider both gas
347   chemistry and particle dynamics, simulations are conducted using boundary conditions
348   and emission rates at five time points (7 a.m., 10 a.m., 1 p.m., 3 p.m. and 5 p.m.). Other
349   simulation conditions, including the grid, coupling method, and time step, are the same
350   as the transient-condition simulation.
351   In Fig. 7, for PM$_{10}$ and NO$_2$, the concentrations simulated with CCM (red triangles) are
352   similar to those simulated with TCM. In addition, depending on the background
353   concentration and emission conditions, the simulation time required for CCM to reach
354   dynamic equilibrium is less than 1000 time steps (approximately 500 s). Therefore, CCM
355   can be utilized for parameter studies. The sensitivity analysis of the grid, coupling method
356   and time step in Section 4.3 and 4.4 is based on CCM. However, CCM should be used
357   with caution when the inflow wind speed and direction vary rapidly. The simulated
358   concentrations in Section 5 are based on TCM.
359

360   *4.3. Grid sensitivity*
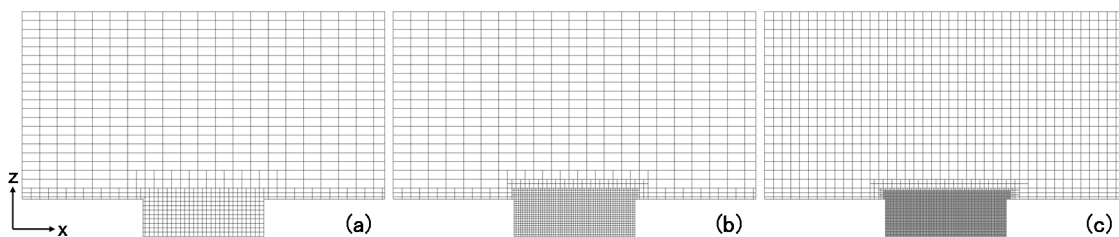
361

362   Fig. 8 Different grid resolutions for sensitivity analysis: (a) coarse, (b) basic, (c) fine. The

363   grid resolutions in the street canyon are 1 m, 0.5 m and 0.25 m in both x-and z- directions,

364   respectively. The largest grid sizes are 4 m (x) $\times$ 2m (z) in the coarse and basic grids,

365   and 2 m (x) $\times$ 2m (z) in the fine grid.

366

367   Grid sensitivity analysis is conducted based on three different resolutions as shown in Fig.

368   8. The grid resolutions in the street canyon for coarse, basic and fine grids are 1 m, 0.5 m

369   and 0.25 m in both x-and z- directions, respectively. The largest grid sizes are 4 m (x) $\times$

370   2m (z) for the coarse and basic grids, and 2 m (x) $\times$ 2m (z) for the fine grid. The

371   simulations are based on constant-condition method. The A-B-A splitting method, which

372   is introduced in Section 4.4, is used with a time step of 0.5 s. Fig. 9 shows the comparative

373   results for the mass concentration. No significant discrepancy is observed between the

374   different grids for NO_2, inert matter and organic matter. Meanwhile, the simulated

375   inorganic matter based on coarse grids shows slightly smaller concentrations than the

376   other grid resolutions, while the concentrations based on basic and fine grids are close.

377   Therefore, the basic grid is adopted for simulations in this study.
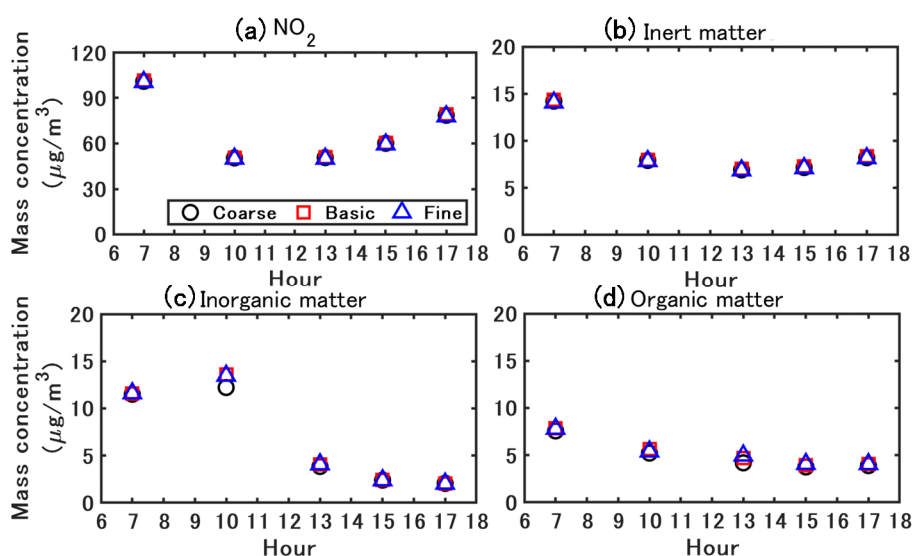
378

379   Fig. 9 Simulated NO_2 and particle concentrations with different grid resolutions.

380

4.4. Coupling method and time step sensitivity

The transport equation for the chemical species includes terms of advection, diffusion, emission and chemical reactions. Ideally, the transport equation should be solved with all the above terms, that is, by coupling all processes. However, the chemical process is integrated with a stiff integrator, whereas advection, diffusion and emission are integrated with a flux scheme. Therefore, operator splitting (Sportisse, 2000) is often employed to solve different terms individually and sequentially over a given time step in chemical transport simulations (Fu and Liang, 2016).

In this study, advection, diffusion and emission are simultaneously solved in CFD, and the chemical reactions including gas chemistry, particle dynamics and size redistribution are solved in SSH-Aerosol. Two operator-splitting orders are considered for coupling: A-B splitting and A-B-A splitting (Sportisse, 2000). For A-B splitting, which can be summarized as CFD(Δt)-Chemistry(Δt), the mass concentrations are first integrated for transport over a time step Δt. The updated concentrations are then integrated for chemistry at the same Δt. On the other side, A-B-A splitting adopts a symmetric sequence of operators, which can be summarized as CFD($\Delta t/2$)-Chemistry(Δt)-CFD($\Delta t/2$). The mass concentrations are first integrated for transport over a half time step, then for chemistry over the full time step and finally for transport again over a half time step.

399

Table 2 Relative change in the computation time with different operator-splitting order and time steps. The computation time is normalized by ABA-05.

Case	Operator splitting order	Δt (s)	Change in the computation time
AB-05	A-B splitting CFD(Δt)-Chemistry(Δt)	0.5	0.90
AB-025		0.25	1.56
ABA-1	A-B-A splitting CFD($\Delta t/2$)-Chemistry(Δt)-CFD($\Delta t/2$)	1	0.57
ABA-05		0.5	1
ABA-025		0.25	2.44

402

A sensitivity analysis is conducted on the operator splitting method and splitting time step. As shown in Table 2, the time step is considered 0.5 s and 0.25 s for the A-B splitting (named AB-05 and AB-025), and 1 s, 0.5 s and 0.25 s for the A-B-A splitting (named ABA-1, ABA-05 and ABA-025). The simulated NO_2 and particle concentrations are presented in Fig. 10. ABA-1 and AB-05 concentrations hardly differ from the figures. Meanwhile, the computational time of ABA-1 is only 63% of that of AB-05. Similarly, the concentrations simulated with ABA-05 and AB-025 are almost the same, and the

410 computational time of ABA-05 is only 64% of AB-025. Therefore, the A-B-A splitting

411 method can be considered as a cost effective method.

412
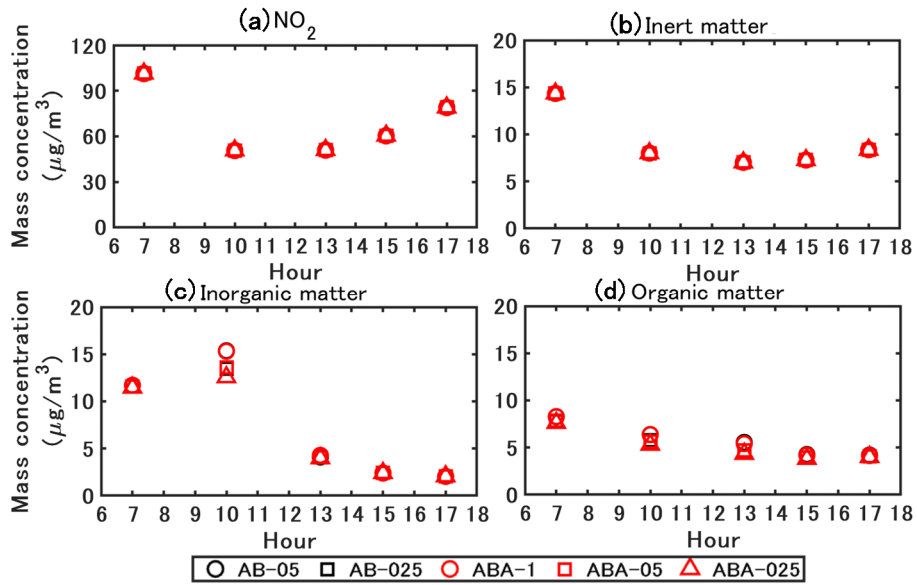
413

414 Fig. 10 Simulated NO_2 and particle concentrations with different coupling methods and

415 time steps. ABA denotes the A-B-A splitting method: CFD(Δt/2)-Chemistry(Δt)-

416 CFD(Δt/2). AB denotes the A-B splitting method: CFD(Δt)-Chemistry(Δt). In the legend,

417 the values that follow the capital letter ABA or AB denote the time step Δt (in s) used in

418 the simulation.

419

420 The concentrations simulated with the A-B-A splitting method and different time steps

421 show that small time step results in low inorganic and organic matter concentrations. The

422 concentrations simulated with ABA-1 are larger than those of ABA-05, and larger than

423 ABA-025. However, the differences between the concentrations simulated with ABA-05

424 and ABA-025 are lower than the differences between ABA-1 and ABA-05. For NO_2 and

425 inert particles, no obvious difference is found between the simulations with different

426 splitting methods and splitting time steps. Therefore, the A-B-A splitting method with a

427 time step of 0.5 s is adopted in this study.

428

5. Results and discussion

5.1. Time-averaged flow field and concentration field
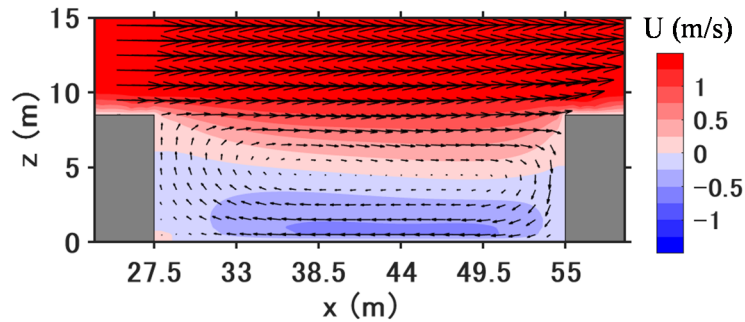
Fig. 11 Time-averaged flow field in the street canyon from 5 a.m. to 5 p.m.

This section shows the results for time-averaged values from 5 a.m. to 5 p.m. Fig. 11 shows the 12-hour time-averaged streamwise velocity and wind direction in the street canyon. At the current aspect ratio (*H*/*W*=0.31), a large vortex is observed in the canyon with a small secondary vortex at the corner of the leeward wall. A reverse flow is observed in the lower half of the canyon.
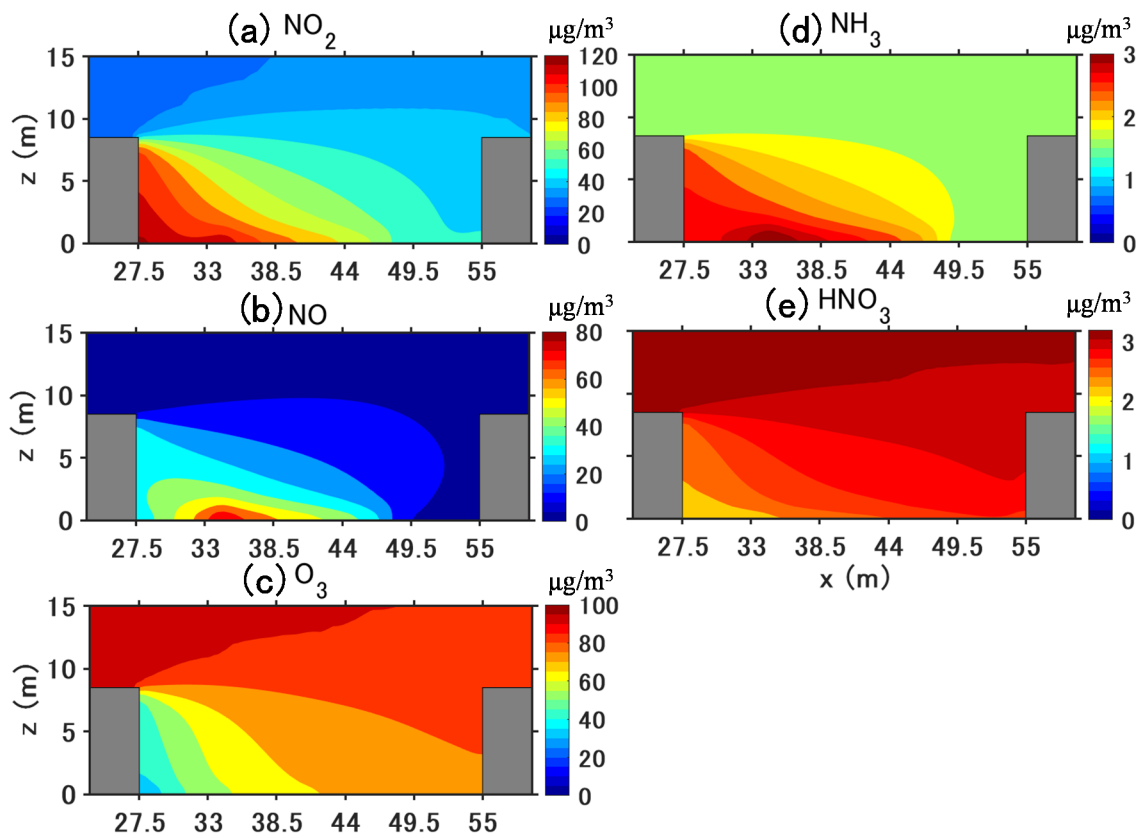
Fig. 12 Time-averaged concentrations ($\mu g/m^3$) of gaseous pollutants in the street canyon

441   from 5 a.m. to 5 p.m.

442

443   Fig. 12 shows the time-averaged concentrations of the gaseous pollutants from 5 a.m. to
444   5 p.m. For gaseous pollutants emitted by traffic, such as NO_2, NO and NH_3, larger
445   concentrations are found in the street, particularly near the leeward wall, compared to the
446   windward wall due to the reverse flow. Simultaneously, gas-phase chemistry and
447   condensation/evaporation between the gas and particle phases also influence the
448   concentration distribution. NO_2 mainly increases due to chemical production from NO
449   emissions and background O_3. Compared to the background NO_2 concentration of 26
450    $\mu g/m^3$, the longest retention time at the leeward side corner leads to the street canyon's
451   largest concentration (121 $\mu g/m^3$). At pedestrian height (z=1.5 m), NO_2 concentration is
452   116 $\mu g/m^3$ at the leeward wall and 49 $\mu g/m^3$ at the windward wall.
453   However, NO and NH_3 generally decrease because of loss by gaseous chemistry and the
454   condensation of ammonium nitrate, respectively; therefore, the largest concentrations are
455   at the leeward corner of the traffic emission source. For secondary gaseous pollutants
456   without traffic emissions such as O_3 and HNO_3, gaseous chemistry and condensation lead
457   to lower concentrations in the street canyon than background concentrations. For O_3, this
458   is due to the titration of O_3 by NO, whose concentration is large near the leeward wall.
459   For HNO_3, this is because of the high concentrations of NH_3, which then condenses with
460   HNO_3 to form ammonium nitrate. In addition, the lowest concentration of O_3 and HNO_3
461   can be found at the leeward corner which corresponds to the secondary vortex in Fig. 11,
462   indicating that the pollutant residence time is the highest in that corner leading to enhance
463   ozone titration.
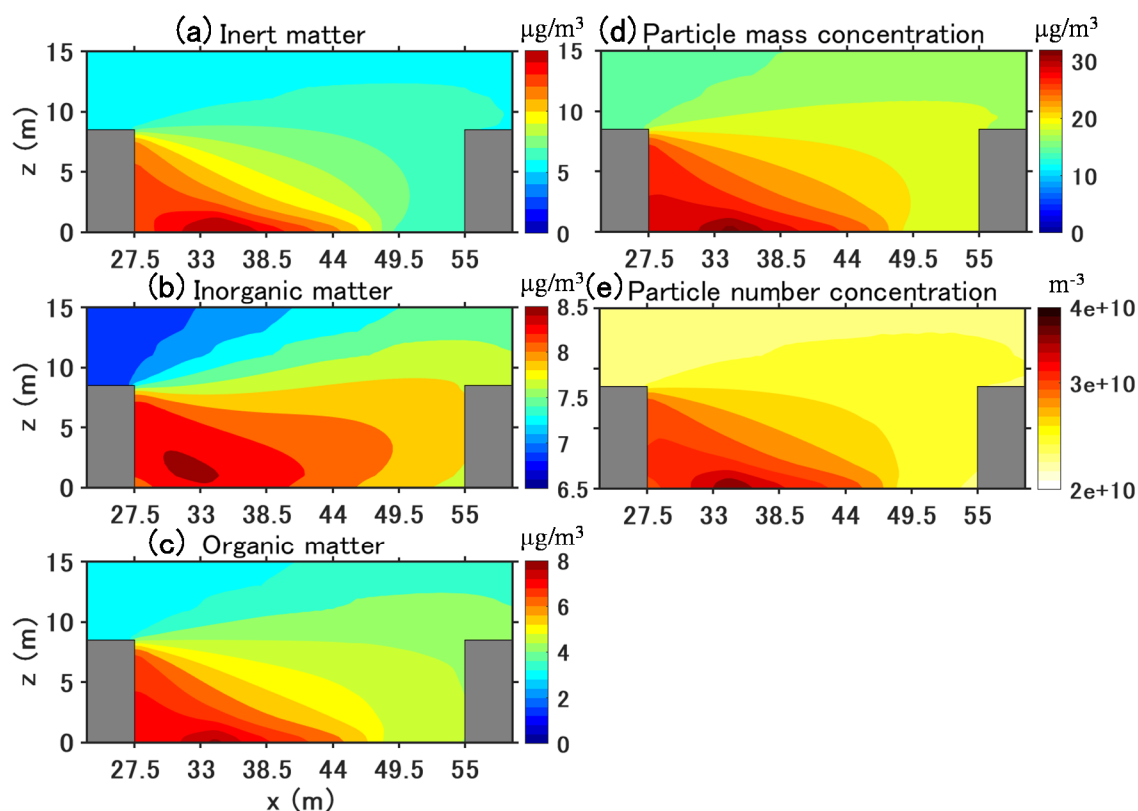
Fig. 13 Time-averaged concentrations of particle number, mass and composition in the street canyon from 5 a.m. to 5 p.m. The unit is μg/m³ for mass concentration and m⁻³ for number concentration.

Fig. 13 shows the time-averaged PM_{10} mass concentration, and the number concentrations and PM composition (inorganic, organic and inert matter) from 5 a.m. to 5 p.m. For inert and organic matter, the highest concentrations are near the leeward corner of the traffic emission source. Because inorganic matter is not emitted, the concentration distribution differs from inert and organic matter. However, as they are produced from gas condensation and strongly influenced by traffic emissions, the highest concentrations are observed in the leeward corner.

At pedestrian height (z=1.5 m), the PM_{10} mass concentration is approximately 28 μg/m³ at the leeward wall and 19 μg/m³ at the windward wall, which is larger than the background concentration of 15 μg/m³. The number concentration is computed from the mass concentration and therefore has a similar spatial distribution as PM_{10} mass concentration (nucleation from gas was not taken into account). Traffic emission significantly increases the number concentration. The number concentration is about 2.3×10^{10} m⁻³ in the background, whereas the largest number concentration in the street canyon is about 3.8×10^{10} m⁻³.

484

5.2. Time-variant characteristics
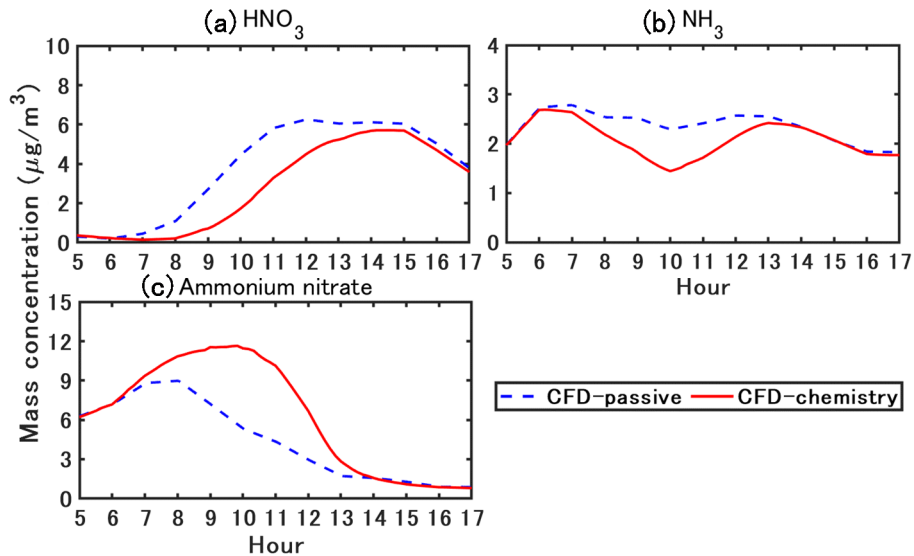
Fig. 14 Simulated time-varying concentrations of ammonium nitrate and precursor gas (HNO$_3$ and NH$_3$).

Fig. 14 shows the simulated time-varying concentrations of ammonium nitrate formed by the condensation of HNO$_3$ and NH$_3$. Based on the traffic fleet in the current study, NH$_3$ emission is approximately 1-2% of NOx emissions. Ammonium nitrate and HNO$_3$ are not emitted and differences between simulations with or without chemistry coupling are due to gas chemical reactions and phase change between the gas and particle. Phase change may be driven by NH$_3$ emissions, as well as the non-thermodynamic equilibrium of the background concentrations.

In CFD-passive, NH$_3$ concentration peaks around 7 a.m. as NOx because it is emitted by traffic. The peak in HNO$_3$ concentration is later in the morning, around 11 am. HNO$_3$ is formed from the oxidation of NO$_2$, which is emitted by traffic and is rapidly formed from NO traffic emissions. The formation of HNO$_3$ is slower than the formation of NO$_2$, and probably occurs at the regional scale, leading to a delay in the peak of HNO$_3$ concentration compared to NO$_2$ concentration. In CFD-chemistry, the temporal variations of HNO$_3$ concentration show large differences with CFD-passive because HNO$_3$ condenses with NH$_3$ to form ammonium nitrate during the daytime. As a result, the HNO$_3$ concentration peak in CFD-chemistry is later than that in CFD-passive (it is shifted from 11 a.m. to around 2 p.m.). The NH$_3$ concentration in CFD-passive peaks at 7 a.m. because of traffic emission and is stable from 7 a.m. to 1 p.m. and then decreases from 1 p.m. Meanwhile, the condensation in CFD-chemistry leads to lower concentration than in

509   CFD-passive during the daytime (between 7 a.m. and 1 p.m.).

510   For 12-hour time-averaged concentrations, ammonium nitrate increases by 46% in CFD-

511   chemistry compared with that in CFD-passive. Background ammonium nitrate

512   concentration (CFD-passive) peaks around the morning rush (7 to 8 a.m.) and then

513   decreases. Meanwhile, in CFD-chemistry, ammonium nitrate concentration peaks later

514   around 10 a.m., because of the large increase in HNO_3 between the traffic rush and 10

515   a.m. However, although HNO_3 concentration does not vary much between 11 a.m. and 3

516   p.m., the ammonium nitrate concentration decreases from 10 a.m. to a very small level

517   (lower than 1 $\mu g/m^3$) after 2 p.m. This decrease is probably linked to the temperature

518   increase during the daytime (Fig. 2(b)) and the relative humidity decrease, leading to a

519   decrease in the condensation rate (Stelson and Seinfeld, 1982).
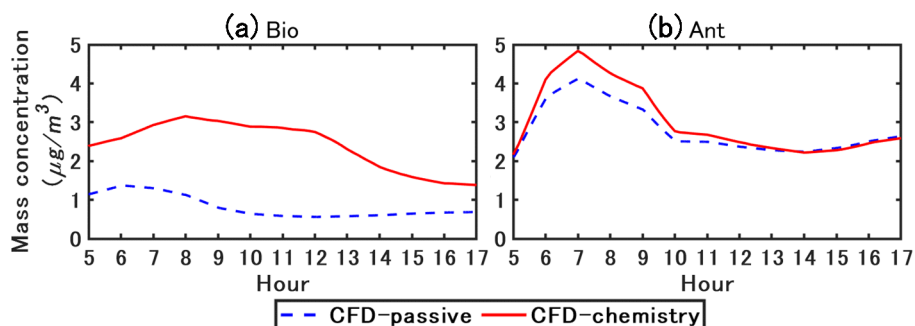
520

521   Fig. 15 Simulated time-varying concentration of organic matter. Bio refers to organic

522   matter formed from biogenic precursors. Ant refers to organic matter formed from

523   anthropogenic precursors.

524

525   Fig. 15 shows the simulated time-varying concentrations of organic matter. Organic

526   matter is divided into two main categories depending on the origin of the precursors: Bio

527   and Ant refer to the organic matter of biogenic and anthropogenic precursors respectively.

528   In CFD-chemistry, Bio concentration is larger than that in CFD-passive. As biogenic

529   precursors are not emitted in the street, the condensation of Bio is due to background

530   precursor gases. As discussed previously, the concentration of ammonium nitrate is higher

531   in CFD-chemistry than in CFD-passive, providing a larger aqueous mass onto which

532   hydrophilic compounds of the biogenic precursor gases condense. As the condensation of

533   ammonium nitrate decreases in the afternoon as shown in Fig. 14, the condensation of

534   Bio also decreases.

535   Ant is largely influenced by traffic emissions in the street, particularly by emissions of

536   semi-volatile compounds (Sartelet et al., 2018), which soon condenses after emissions.

537   Therefore there is a peak around 7 a.m. owing to the morning rush. In the model,

538   anthropogenic emissions are mostly hydrophobic, therefore the condensation is not

539 enhanced by the increase in inorganic concentrations. Consequently, the difference
540 between CFD-chemistry and CFD-passive is larger in the morning owing to the large
541 increase in traffic emissions, but small differences are observed in the afternoon.
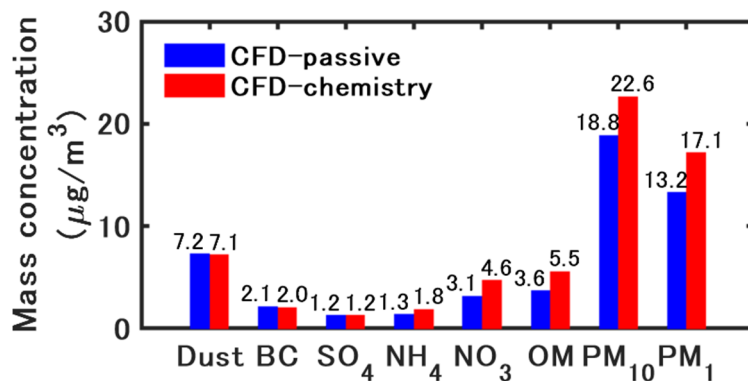
542
543 Fig. 16 Time-averaged concentration of PM_{10}, PM_1 and the chemical compounds of PM_{10}
544 from 5 a.m. to 5 p.m.

545

546 Fig. 16 shows the time-averaged concentrations of PM_{10}, PM_1 and the chemical
547 compounds of PM_{10} from 5 a.m. to 5 p.m. The time-averaged PM_{10} and PM_1
548 concentrations increase by approximately 3.8 $\mu g/m^3$ in CFD-chemistry compared to CFD-
549 passive, indicating that chemistry mainly influences small particles. Inert matter slightly
550 decreases in CFD-chemistry owing to dry deposition. Condensation increases of 48%,
551 38% and 53% of nitrate, ammonium and organic matter concentrations in CFD-chemistry
552 compared to CFD-passive.

553

554   *5.3. Size distribution of particle matter*

555
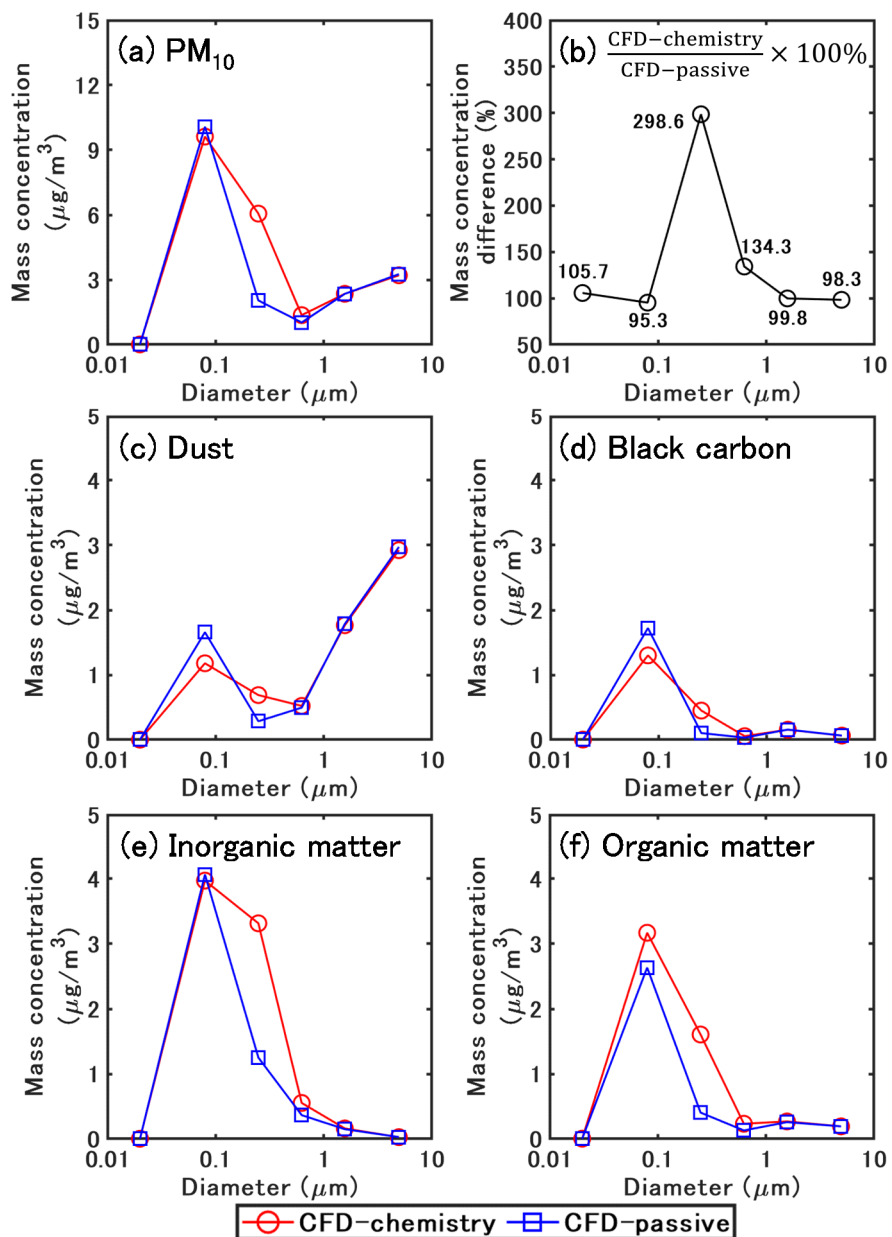
Fig. 17 Time-averaged size distribution of PM_{10} for different chemical species from 5 a.m.

to 5 p.m.

558

Fig. 17 shows the time-averaged size distribution of PM_{10} for the different chemical compounds of particles from 5 a.m. to 5 p.m. The bound diameters are 0.01, 0.04, 0.16, 0.4, 1.0, 2.5 and 10 μm, and the mean diameters are 0.02, 0.08, 0.25, 0.63, 1.58 and 5.01 μm.

For the total concentration of PM_{10} (Fig. 17(a)), the lowest and the largest concentrations are in the first size section (0.01-0.04 μm) and the second size section (0.04-0.16 μm)

565   respectively, for both the CFD-passive and the CFD-chemistry simulations. Generally,
566   the loss and gain of mass concentration in each size section are related to emission, dry
567   deposition, coagulation (small particles coagulate into large particles), and
568   condensation/evaporation (phase exchange between gas and particles).
569   Fig. 17(b) shows the mass concentration ratio between CFD-passive and CFD-chemistry
570   for each size section. For particles in the size range of 0.04-0.16 μm, the concentrations
571   are smaller in CFD-chemistry than in CFD-passive, because dry deposition and
572   coagulation both decrease mass concentration for those particles. Furthermore, semi-
573   volatile gases may evaporate from small particles because of the Kelvin effect and
574   condense onto larger particles. For particles in the size range of 0.16-1.0 μm, the
575   concentrations are much larger in CFD-chemistry than CFD-passive, indicating that
576   coagulation and condensation on the mass-concentration increase are dominant to other
577   processes, such as deposition. For particles larger than 1 μm, the concentrations of CFD-
578   passive and CFD-chemistry are similar, because particle dynamics have a low influence
579   on large particles.
580   The size distribution of dust (Fig. 17(c)) shows that most dust mass concentrations are in
581   particles larger than 1 μm. Meanwhile, most of the mass concentration of BC, inorganic
582   and organic matter (Fig. 17(d-f)) is in particles smaller than 1 μm. Coagulation is the main
583   process influencing the size distribution for inert matter (dust and BC). Compared to
584   CFD-passive, the mass concentration of dust and BC in the second size section decrease
585   by 0.48 and 0.43 μg/m^3 in CFD-chemistry. Correspondingly, the mass concentrations of
586   dust and BC in the third size section increase by 0.41 and 0.35 μg/m^3.
587   For inorganic matter, in the second size section, the concentrations are similar in CFD-
588   passive and CFD-chemistry: particle dynamics decrease sulphate concentration by 0.32
589   μg/m^3 and increase nitrate concentration by 0.17 μg/m^3. However, as the results of the
590   combination effect of coagulation and ammonium nitrate condensation, the
591   concentrations largely increase in the third size section in CFD-chemistry: sulphate,
592   ammonium and nitrate increase by 0.27, 0.6 and 1.24 μg/m^3, respectively.
593   For organic matter, because of condensation of hydrophilic compounds from background
594   biogenic gases and anthropogenic emissions, CFD-chemistry leads to a small increase in
595   concentrations (0.53 μg/m^3) in the second size section and a large increase in the third
596   section (1.21 μg/m^3) compared to CFD-passive. In detail, Bio concentrations increase by
597   0.89 μg/m^3, and Ant concentrations decrease by 0.36 μg/m^3 in the second size section. In
598   the third size section, Bio and Ant concentrations increase by 0.67, 0.54 μg/m^3.
599

600   *5.4. Influence of ammonia traffic emissions*
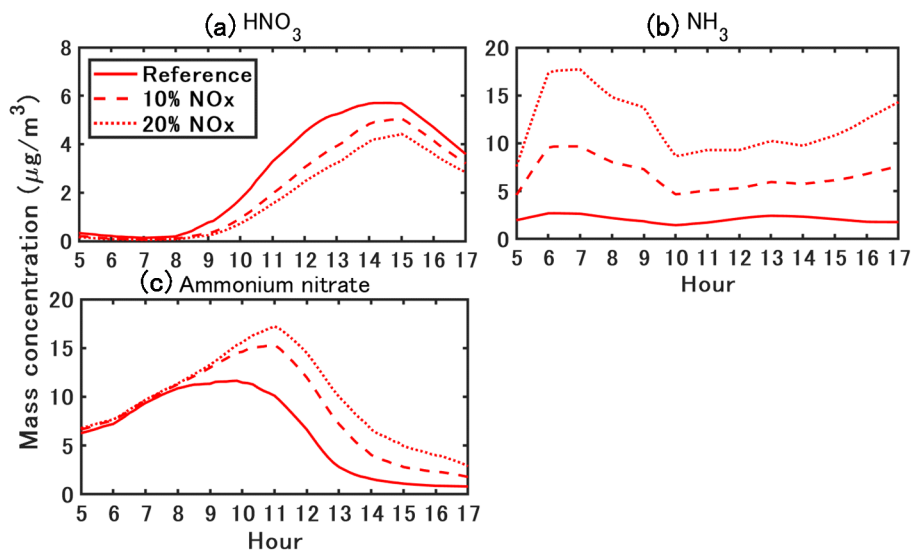
602   Fig. 18 Sensitivity of ammonium nitrate concentration to NH$_3$ emission.

603

604   Suarez-Bertoa et al. (2017) conducted on-road measurements of NH$_3$ emissions from two
605   Euro 6b compliant light duty cars (one gasoline and one diesel) under real-world driving
606   conditions, and they found that NH$_3$ emissions accounted for 11.9% and 0.92% of NOx
607   emissions for gasoline and diesel vehicles. As explained in Section 5.2, NH$_3$ emission
608   emissions are approximately 1-2% of NOx emissions in the reference case. Two cases are
609   considered to simulate the impact of an increase in the fraction of gasoline cars, and
610   sensitivity simulations are performed with NH$_3$ emission considered as 10% and 20% of
611   the NOx emissions.

612   Fig. 18 shows the sensitivity of ammonium nitrate concentration to NH$_3$ emissions. A
613   larger NH$_3$ emission delays the peak of ammonium nitrate by approximately one hour.
614   For a 12-hour average, considering NH$_3$ emissions of 10% and 20% of NOx emissions
615   leads to a large increase in ammonium nitrate (35% and 55%) compared to the reference
616   case, because of the formation of ammonium nitrate by the condensation of HNO$_3$ and
617   NH$_3$.

618

619   **6. Conclusions**

620   Particles in urban environment impose adverse impacts on pedestrians' health.
621   Conventional CFD methods regarding particles as passive scalars cannot reproduce the
622   formation of secondary aerosols and may lead to uncertain simulations. Therefore, to
623   increase the simulation accuracy of particle dispersion, we coupled the CFD software
624   OpenFOAM (OF) and Code_Saturne (CS) with SSH-Aerosol, a modular box model to

625   simulate the evolution of primary and secondary aerosols. The main processes involved
626   in the aerosol dynamics (coagulation, condensation /evaporation and dry deposition) were
627   considered.
628   We simulated a 12-hour transient dispersion of pollutants from traffic emissions in a street
629   canyon using the unsteady RANS model. The simulation domain was generated to model
630   a street-canyon where field measurements are available. The flow field was based on the
631   WRF model. The background concentrations of gas and particles were obtained from
632   regional-scale simulations with a chemistry-transport model. The particle diameter range
633   (0.01 μm to 10 μm) was divided into six size sections. The following conclusions were
634   drawn from the results of this study.

635   1)   The simulated spatially-averaged values in the street canyon were validated from
636   field measurement using validation metrics. For both OF and CS, the simulated NO_2
637   and PM_{10} concentrations based on the coupling model (CFD-chemistry) achieved
638   better agreement with the measurement data than the conventional CFD simulation
639   which considered pollutants as passive scalars (CFD-passive). The differences
640   between of the OF and CS results were not obvious and were mainly due to the
641   differences in the turbulence scheme. The following conclusions were drawn based
642   on the simulated OF concentrations.

643   2)   For the flow field, a large vortex was observed in the canyon with a small secondary
644   vortex at the corner of the leeward wall at the current aspect ratio (H/W=0.31). In
645   CFD-chemistry, because of the reverse flow, the 12-hour (from 5 a.m. to 5 p.m.) time-
646   averaged NO_2 mass concentration, PM_{10} mass and number concentrations at
647   pedestrian height were much higher near the leeward wall (116 μg/m^3, 28 μg/m^3,
648   3.2×10^{10} m^{-3}) than the background (26 μg/m^3, 15 μg/m^3, 2.3×10^{10} m^{-3}).

649   3)   Secondary aerosol formation largely affected the mass concentration and size
650   distribution of particle matter. For 12-hour time-averaged concentrations, ammonium
651   nitrate and organic matter increased by 46% and 53% in CFD-chemistry compared
652   to CFD-passive because of condensation of HNO_3 and NH_3, background biogenic
653   precursor-gases and anthropogenic precursor-gas emissions. Coagulation largely
654   influenced the size distribution of small particles by combining particles with a
655   diameter of 0.04-0.16 μm into 0.16-0.4 μm. At the same time, CFD-chemistry
656   showed a much larger concentration than CFD-passive for the particles in 0.16-1.0
657   μm, indicating that the effect of condensation on increasing mass concentration was
658   dominant compared to other chemical processes.

659   4)   Urban areas are NH_3-limited (HNO_3 sufficient) areas, therefore, increasing NH_3 leads
660   to a large increase in ammonium nitrate. Vehicles are considered to be the main

661 source of NH$_3$ in urban environments. Increasing the fleet's proportion of recent
662 gasoline vehicles may increase NH$_3$ emissions. For a 12-hour average, we considered
663 NH$_3$ emissions of 10% and 20% of NOx emissions led to a large increase in
664 ammonium nitrate (35% and 55%) compared to the reference case which considers
665 NH$_3$ emission as 1-2% of NOx emissions.

666 5) A grid sensitivity analysis showed that the particles' concentrations of inorganic and
667 organic compounds were sensitive to grid resolution, whereas inert particle
668 concentrations were not sensitive to grid resolution. In addition, simulated values
669 based on a grid size of 0.5 m in the street canyon showed small differences with a
670 grid size of 0.25 m, indicating that a spatial resolution of 0.5 m can be enough for
671 reactive particle dispersion at the street level.

672 6) Operator splitting is often employed to solve the transport term and chemical
673 reactions over a given time step in chemical transport simulations. Two integration
674 orders were considered: A-B splitting method (CFD(Δt)-Chemistry(Δt)) and A-B-A
675 splitting method (CFD(Δt/2)-Chemistry(Δt)-CFD(Δt/2)). The results showed that
676 the A-B-A splitting method had almost the same concentrations as the A-B splitting
677 method with half the computational time. Further sensitivity analysis on the time step
678 showed that a time step of 0.5 s was enough when using the A-B-A splitting method.

679 7) Conducting a CFD simulation with constant boundary conditions and emission rates
680 at a specific time point is considered a practical method to achieve time-averaged
681 concentrations for evaluating street-level pollutant concentrations. The validation
682 was conducted using conditions on five time points (7 a.m., 10 a.m., 1 p.m., 3 p.m.
683 and 5 p.m.). The simulated concentration based on the above method exhibited
684 almost the same value as the simulation with transient conditions at the same time
685 points.

686 The limitation of this study should be addressed as several reasonable approximations
687 and assumptions were made in the simulation settings.

688 1) Concerning the simulation domain: since we focused on the coupling of gas chemical
689 reactions and particle dynamics to the CFD codes, we selected a 12-hour period when
690 wind direction was perpendicular to the street. In that case, a 2-D simplification of
691 the simulation domain is reasonable, as shown by Maison et al. (2022). However, in
692 more general cases, the pollutant residence time for a 3-D canyon could be shorter
693 compared to the 2-D canyon adopted in this study, and the effects of chemical
694 reaction or aerosol processes could be weaker than this study reported. In addition,
695 various wind directions should be considered to better evaluate the performance of
696 the coupled model. Further work will focus on the application of the coupled model

697   to a complex urban environment with changing wind directions.

698   2) Concerning the physical model: the simulations were based on RANS-closure, and

699   the SSH-aerosol processed the ensemble-averaged concentration, therefore the

700   covariance of turbulent diffusion and chemical reaction may not be fully reproduced.

701   The simulation based on LES may provide better prediction of second-order

702   quantities. In addition, the radiation on the wall may lead street-level-variations of

703   temperature and could affect the flow field and chemical reaction rates. However,

704   this was not considered here, and the radiation effect on the local temperature was

705   simplified as being the same as in the inflow condition. The inflow temperature was

706   obtained from WRF model where the radiation was considered, and the time variation

707   of temperature was considered to be the same as the background.

708 Future work will be conducted on the influence of environmental factors and emission

709 conditions, aiming to provide knowledge to devise suitable countermeasures to decrease

710 particle concentration in microscale urban environments.

711

712 Acknowledgments: This work benefited from discussions with Bertrand Carissimo. The

713 authors acknowledge funding from DIM QI^2 (Air Quality Research Network on air

714 quality in the Île-de-France region) and from Île-de-France region.

715

716 Code/Data availability

717 The codes used in this publication are available to the community, and they can be

718 accessed by request to the corresponding author.

719

720 Author contribution

721 KS and RO were responsible for conceptualization. CL, YW, CF, KS, YK and ZW

722 developed the software. CL and YW conduced the visualization and validation; CL, YW

723 and KS performed the formal analysis. KS and RO acquired resources. CL, YW, RO and

724 KS were responsible for writing and original draft preparation. CF, YK, HK reviewed and

725 edited the manuscript All co-authors contributed to the discussion of the paper.

726

727 Competing interests

728 The contact author has declared that neither they nor their co-authors have any

729 competing interests.

730

731 Reference

732 Anenberg, S. C., Miller, J., Minjares, R., Du, L., Henze, D. K., Lacey, F., Malley, C. S.,

733 Emberson, L., Franco, V., Klimont, Z., and Heyes, C.: Impacts and mitigation of excess
734 diesel-related NO x emissions in 11 major vehicle markets, Nature, 545, 467–471,
735 https://doi.org/10.1038/nature22086, 2017.

736 EMEP/EEA: EMEP/EEA air pollutant emission inventory guidebook 2019, EEA Report
737 No 13/2019, European Environment Agency:
738 https://www.eea.europa.eu/publications/emep-eea-guidebook-2019, last access: 14
739 March 2022.

740 Archambeau, F., Méchitoua, N., and Sakiz, M.: Code Saturne: A Finite Volume Code for
741 Turbulent flows - Industrial Applications, International Journal on Finite Volumes, 1,
742 2004.

743 Arpaci, V. S. and Larsen, P. S.: Convection Heat Transfer, Prentice Hall, New York,
744 1984.

745 Belcher, S. E.: Mixing and transport in urban areas, Philosophical Transactions of the
746 Royal Society A: Mathematical, Physical and Engineering Sciences, 363, 2947–2968,
747 https://doi.org/10.1098/rsta.2005.1673, 2005.

748 Bishop, G. A. and Stedman, D. H.: Reactive Nitrogen Species Emission Trends in Three
749 Light-/Medium-Duty United States Fleets, Environ Sci Technol, 49, 11234–11240,
750 https://doi.org/10.1021/acs.est.5b02392, 2015.

751 Blackman, K., Perret, L., and Savory, E.: Effect of upstream flow regime on street
752 canyon flow mean turbulence statistics, Environmental Fluid Mechanics, 15, 823–849,
753 https://doi.org/10.1007/s10652-014-9386-8, 2015.

754 Blocken, B., Tominaga, Y., and Stathopoulos, T.: CFD simulation of micro-scale
755 pollutant dispersion in the built environment, Build Environ, 64, 225–230,
756 https://doi.org/10.1016/j.buildenv.2013.01.001, 2013.

757 Boutahar, J., Lacour, S., Mallet, V., Quelo, D., Roustan, Y., and Sportisse, B.:
758 Development and validation of a fully modular platform for numerical modelling of air
759 pollution: POLAIR, Int J Environ Pollut, 22, 17,
760 https://doi.org/10.1504/IJEP.2004.005474, 2004.

761 Chang, J. C. and Hanna, S. R.: Air quality model performance evaluation, Meteorology
762 and Atmospheric Physics, 87, 167–196, https://doi.org/10.1007/s00703-003-0070-7,
763 2004.

764 Du, Y., Xu, X., Chu, M., Guo, Y., and Wang, J.: Air particulate matter and
765 cardiovascular disease: The epidemiological, biomedical and clinical evidence,
766 https://doi.org/10.3978/j.issn.2072-1439.2015.11.37, 2016.

767 Ferrero, E., Alessandrini, S., Anderson, B., Tomasi, E., Jimenez, P., and Meech, S.:
768 Lagrangian simulation of smoke plume from fire and validation using ground-based

769   lidar and aircraft measurements, Atmos Environ, 213, 659–674,

770   https://doi.org/10.1016/j.atmosenv.2019.06.049, 2019.

771   Fu, K. and Liang, D.: The conservative characteristic FD methods for atmospheric

772   aerosol transport problems, J Comput Phys, 305, 494–520,

773   https://doi.org/10.1016/j.jcp.2015.10.049, 2016.

774   Gao, S., Kurppa, M., Chan, C. K., and Ngan, K.: Technical note: Dispersion of cooking-

775   generated aerosols from an urban street canyon, Atmos Chem Phys, 22, 2703–2726,

776   https://doi.org/10.5194/acp-22-2703-2022, 2022.

777   Guimet, V. and Laurence, D.: A linearised turbulent production in the k-ε model for

778   engineering applications, in: Engineering Turbulence Modelling and Experiments 5,

779   edited by: Rodi, W. and Fueyo, N., Elsevier Science Ltd, Oxford, UK, 157–166, 2002.

780   Hanna, S. R., Hansen, O. R., and Dharmavaram, S.: FLACS CFD air quality model

781   performance evaluation with Kit Fox, MUST, Prairie Grass, and EMU observations,

782   Atmos Environ, 38, 4675–4687, https://doi.org/10.1016/j.atmosenv.2004.05.041, 2004.

783   Harten, A.: On a Class of High Resolution Total-Variation-Stable Finite-Difference

784   Schemes, SIAM J Numer Anal, 21, 1–23, https://doi.org/10.1137/0721001, 1984.

785   Jones, A. M., Yin, J., and Harrison, R. M.: The weekday–weekend difference and the

786   estimation of the non-vehicle contributions to the urban increment of airborne

787   particulate matter, Atmos Environ, 42, 4467–4479,

788   https://doi.org/10.1016/j.atmosenv.2008.02.001, 2008.

789   Kim, M. J.: Sensitivity of nitrate aerosol production to vehicular emissions in an urban

790   street, Atmosphere (Basel), 10, 212, https://doi.org/10.3390/ATMOS10040212, 2019.

791   Kim, M. J., Park, R. J., Kim, J. J., Park, S. H., Chang, L. S., Lee, D. G., and Choi, J. Y.:

792   Computational fluid dynamics simulation of reactive fine particulate matter in a street

793   canyon, Atmos Environ, 209, 54–66, https://doi.org/10.1016/j.atmosenv.2019.04.013,

794   2019.

795   Kim, Y., Wu, Y., Seigneur, C., and Roustan, Y.: Multi-scale modeling of urban air

796   pollution: development and application of a Street-in-Grid model (v1.0) by coupling

797   MUNICH (v1.0) and Polair3D (v1.8.1), Geosci Model Dev, 11, 611–629,

798   https://doi.org/10.5194/gmd-11-611-2018, 2018.

799   Kim, Y., Lugon, L., Maison, A., Sarica, T., Roustan, Y., Valari, M., Zhang, Y., André,

800   M., Sartelet, K., Paris-saclay, U., and Ecosys, U. M. R.: MUNICH v2.0: A street-

801   network model coupled with SSH-aerosol (v1.2) for multi-pollutant modelling, Geosci

802   Model Dev, 2022.

803   Kumar, P., Fennell, P., Langley, D., and Britter, R.: Pseudo-simultaneous measurements

804   for the vertical variation of coarse, fine and ultrafine particles in an urban street canyon,

Atmos Environ, 42, 4304–4319, https://doi.org/10.1016/j.atmosenv.2008.01.010, 2008.

Kurppa, M., Hellsten, A., Roldin, P., Kokkola, H., Tonttila, J., Auvinen, M., Kent, C., Kumar, P., Maronga, B., and Järvi, L.: Implementation of the sectional aerosol module SALSA2.0 into the PALM model system 6.0: Model development and first evaluation, Geosci Model Dev, 12, 1403–1422, https://doi.org/10.5194/gmd-12-1403-2019, 2019.

Lo, K. W. and Ngan, K.: Characterising the pollutant ventilation characteristics of street canyons using the tracer age and age spectrum, Atmos Environ, 122, 611–621, https://doi.org/10.1016/j.atmosenv.2015.10.023, 2015.

Lo, K. W. and Ngan, K.: Characterizing ventilation and exposure in street canyons using Lagrangian particles, J Appl Meteorol Climatol, 56, 1177–1194, https://doi.org/10.1175/JAMC-D-16-0168.1, 2017.

Lugon, L., Vigneron, J., Debert, C., Chrétien, O., and Sartelet, K.: Black carbon modeling in urban areas: investigating the influence of resuspension and non-exhaust emissions in streets using the Street-in-Grid model for inert particles (SinG-inert), Geosci Model Dev, 14, 7001–7019, https://doi.org/10.5194/gmd-14-7001-2021, 2021a.

Lugon, L., Sartelet, K., Kim, Y., Vigneron, J., and Chretien, O.: Simulation of primary and secondary particles in the streets of Paris using MUNICH, Faraday Discuss, 226, 432–456, https://doi.org/10.1039/d0fd00092b, 2021b.

Maison, A., Flageul, C., Carissimo, B., Wang, Y., Tuzet, A., and Sartelet, K.: Parameterizing the aerodynamic effect of trees in street canyons for the street network model MUNICH using the CFD model Code_Saturne, Atmos Chem Phys, 22, 9369–9388, https://doi.org/10.5194/acp-22-9369-2022, 2022.

OpenFOAM user guide: https://www.openfoam.com/.

Parente, A., Gorlé, C., van Beeck, J., and Benocci, C.: Improved k–ε model and wall function formulation for the RANS simulation of ABL flows, Journal of Wind Engineering and Industrial Aerodynamics, 99, 267–278, https://doi.org/10.1016/j.jweia.2010.12.017, 2011.

Di Sabatino, S., Buccolieri, R., Pulvirenti, B., and Britter, R.: Simulations of pollutant dispersion within idealised urban-type geometries with CFD and integral models, Atmos Environ, 41, 8316–8329, https://doi.org/10.1016/j.atmosenv.2007.06.052, 2007.

Sartelet, K., Zhu, S., Moukhtar, S., André, M., André, J. M., Gros, V., Favez, O., Brasseur, A., and Redaelli, M.: Emission of intermediate, semi and low volatile organic compounds from traffic and their impact on secondary organic aerosol concentrations over Greater Paris, Atmos Environ, 180, 126–137, https://doi.org/10.1016/j.atmosenv.2018.02.031, 2018.

Sartelet, K., Couvidat, F., Wang, Z., Flageul, C., and Kim, Y.: SSH-aerosol v1.1: A

841 modular box model to simulate the evolution of primary and secondary aerosols,

842 Atmosphere (Basel), 11, 525, https://doi.org/10.3390/atmos11050525, 2020.

843 Sartelet, K. N., Debry, E., Fahey, K., Roustan, Y., Tombette, M., and Sportisse, B.:

844 Simulation of aerosols and gas-phase species over Europe with the Polyphemus system:

845 Part I-Model-to-data comparison for 2001, Atmos Environ, 41, 6116–6131,

846 https://doi.org/10.1016/j.atmosenv.2007.04.024, 2007.

847 Sportisse, B.: An Analysis of Operator Splitting Techniques in the Stiff Case, J Comput

848 Phys, 161, 140–168, https://doi.org/10.1006/jcph.2000.6495, 2000.

849 Stelson, A. W. and Seinfeld, J. H.: Relative humidity and temperature dependence of the

850 ammonium nitrate dissociation constant, Atmospheric Environment (1967), 16, 983–

851 992, https://doi.org/10.1016/0004-6981(82)90184-6, 1982.

852 Suarez-Bertoa, R. and Astorga, C.: Impact of cold temperature on Euro 6 passenger car

853 emissions, Environmental Pollution, 234, 318–329,

854 https://doi.org/10.1016/j.envpol.2017.10.096, 2018.

855 Suarez-Bertoa, R., Mendoza-Villafuerte, P., Riccobono, F., Vojtisek, M., Pechout, M.,

856 Perujo, A., and Astorga, C.: On-road measurement of NH 3 emissions from gasoline and

857 diesel passenger cars during real world driving conditions, Atmos Environ, 166, 488–

858 497, https://doi.org/10.1016/j.atmosenv.2017.07.056, 2017.

859 Sun, K., Tao, L., Miller, D. J., Pan, D., Golston, L. M., Zondlo, M. A., Griffin, R. J.,

860 Wallace, H. W., Leong, Y. J., Yang, M. M., Zhang, Y., Mauzerall, D. L., and Zhu, T.:

861 Vehicle Emissions as an Important Urban Ammonia Source in the United States and

862 China, Environ Sci Technol, 51, 2472–2481, https://doi.org/10.1021/acs.est.6b02805,

863 2017.

864 Sung, J. C., Pulliam, B. L., and Edwards, D. A.: Nanoparticles for drug delivery to the

865 lungs, Trends Biotechnol, 25, 563–570, https://doi.org/10.1016/j.tibtech.2007.09.005,

866 2007.

867 Tominaga, Y. and Stathopoulos, T.: Turbulent Schmidt numbers for CFD analysis with

868 various types of flowfield, Atmos Environ, 41, 8091–8099,

869 https://doi.org/10.1016/j.atmosenv.2007.06.054, 2007.

870 Tominaga, Y. and Stathopoulos, T.: CFD simulation of near-field pollutant dispersion in

871 the urban environment: A review of current modeling techniques, Atmos Environ, 79,

872 716–730, https://doi.org/10.1016/j.atmosenv.2013.07.028, 2013.

873 Trini Castelli, S., Armand, P., Tinarelli, G., Duchenne, C., and Nibart, M.: Validation of

874 a Lagrangian particle dispersion model with wind tunnel and field experiments in urban

875 environment, Atmos Environ, 193, 273–289,

876 https://doi.org/10.1016/j.atmosenv.2018.08.045, 2018.

877   Wesely, M. L.: Parameterization of surface resistances to gaseous dry deposition in

878   regional-scale numerical models, Atmospheric Environment (1967), 23, 1293–1304,

879   https://doi.org/10.1016/0004-6981(89)90153-4, 1989.

880   Wu, L., Hang, J., Wang, X., Shao, M., and Gong, C.: APFoam 1.0: Integrated

881   computational fluid dynamics simulation of O3-NOx-volatile organic compound

882   chemistry and pollutant dispersion in a typical street canyon, Geosci Model Dev, 14,

883   4655–4681, https://doi.org/10.5194/gmd-14-4655-2021, 2021.

884   Yakhot, V., Orszag, S. A., Thangam, S., Gatski, T. B., and Speziale, C. G.: Development

885   of turbulence models for shear flows by a double expansion technique, Physics of Fluids

886   A, 4, 1510–1520, https://doi.org/10.1063/1.858424, 1992.

887   Yee, H. C.: Construction of explicit and implicit symmetric TVD schemes and their

888   applications, J Comput Phys, 68, 151–179, https://doi.org/10.1016/0021-

889   9991(87)90049-0, 1987.

890   Zhang, K., Chen, G., Zhang, Y., Liu, S., Wang, X., Wang, B., and Hang, J.: Integrated

891   impacts of turbulent mixing and NOX-O3 photochemistry on reactive pollutant

892   dispersion and intake fraction in shallow and deep street canyons, Science of The Total

893   Environment, 712, 135553, https://doi.org/10.1016/j.scitotenv.2019.135553, 2020.

894   Zhang, L., Gong, S., Padro, J., and Barrie, L.: A size-segregated particle dry deposition

895   scheme for an atmospheric aerosol module, Atmos Environ, 35, 549–560,

896   https://doi.org/10.1016/S1352-2310(00)00326-5, 2001.

897   Zhang, L., Brook, J. R., and Vet, R.: A revised parameterization for gaseous dry

898   deposition in air-quality models, Atmos Chem Phys, 3, 2067–2082,

899   https://doi.org/10.5194/acp-3-2067-2003, 2003.

900

901   Appendix A

902   The schemes for particle deposition velocity v_d were added to the transport equations

903   using volume sink terms based on (Zhang et al., 2001) and can be represented as:

$$v_{d,p} = \begin{cases} v_g + \dfrac{1}{R_a + R_s}, & \text{Wall surfaces} \\ v_g, & \text{Entire field} \end{cases} \qquad (A1)$$

$$v_g = \frac{\rho d_p^2 g C}{18\eta} \qquad (A2)$$

$$R_a = \frac{\ln(z_R/z_0) - \psi_H}{\kappa u_*} \qquad (A3)$$

$$R_s = \frac{1}{\varepsilon_0 u_*(E_B + E_{IM} + E_{IN})R_1} \qquad \text{(A4)}$$

904   The deposition velocity for the particles $v_{d,p}$ consists of both gravitational settling and
905   surface deposition near the wall surfaces. The gravitational settling velocity v_g was
906   considered for the entire field, ρ is the particle density; d_p is the particle diameter; g
907   is the acceleration of gravity; C is Cunningham correction factor for small particles; η
908   is the viscosity coefficient of air.

909   The aerodynamic resistance R_a is calculated from the first-layer-height z_R, roughness
910   length z_0, Von Kármán constant κ, friction velocity u_* and stability function ψ_H. For the
911   k–ε model, u_* is estimated by $\left(C_\mu^{0.5}k\right)^{0.5}$ and $C_\mu = 0.09$ is a constant of the model.

912   The surface resistance R_s is calculated from u_*, the collection efficiency from Brownian
913   diffusion E_B, the impaction E_{IM} and the interception E_{IN}. The correction factor
914   represents the fraction of particles that stick to the surface R_1 and an empirical
915   constant $\varepsilon_0 = 3$.

916   The dry deposition schemes for gas were added to the transport equations using volume
917   sink terms based on (Wesely, 1989) and (Zhang et al., 2003),which can be represented as:

$$v_{d,g} = \frac{1}{R_a + R_b + R_c} \qquad \text{(A5)}$$

$$R_b = \frac{2}{\kappa u_*}\left(\frac{Sc}{Pr}\right)^{2/3} \qquad \text{(A6)}$$

918   The deposition velocity for gas $v_{d,g}$ is calculated from the aerodynamic resistance R_a,
919   the quasi-laminar layer resistance R_b and the surface resistance for gas R_c. $Sc = v/D$
920   and $Pr = 0.72$ are the Schmidt and Prandtl number. v is the kinematic viscosity of air
921   and D is the molecular diffusivity of different gases. R_c is calculated based on (Zhang
922   et al., 2003).

923

924 Appendix B

925 8H with two blocks at intervals of 3H
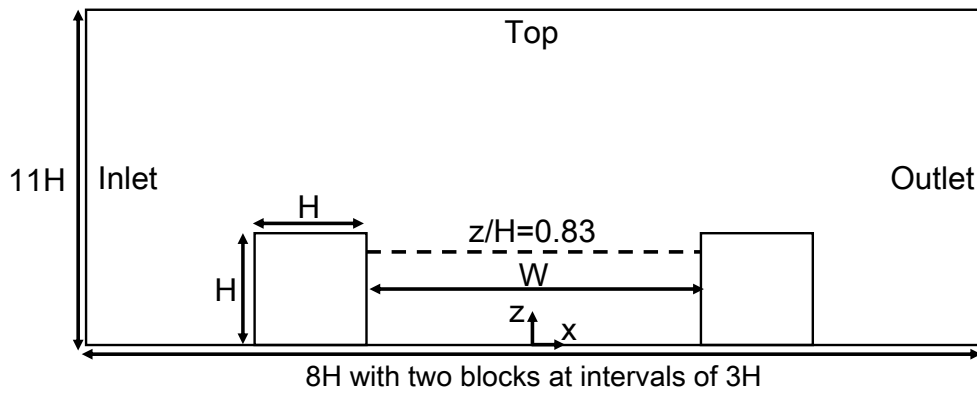
926 Fig. S1 Simulation domain for velocity validation.

927

928 Correctly representing the flow field in the street canyon is important to model accurately
929 the concentrations. Unfortunately, observation data on wind velocity is the street is not
930 available. Therefore, we conducted a velocity validation for OpenFOAM v2012 using
931 data from a wind tunnel experiment (Blackman et al., 2015). The 2-D simulation domain
932 is shown in Fig. S1. The aspect ratio in the experiment (H/W=0.33) is close to this study
933 (H/W=0.31). The building height H is 0.06 m. The grid size is 1/20 H in x- and z-
934 directions in the simulation domain under $3H$. The free-stream velocity U_{ref} is 5.9 m/s.
935 The steady-state flow field is simulated with the same turbulence model (RNG k–ε model)
936 as in the paper, and cyclic boundary conditions are used for the inlet and outlet. The slip
937 boundary is considered for the top, and non-slip boundary conditions with the same wall
938 functions as in the paper are considered for other walls.
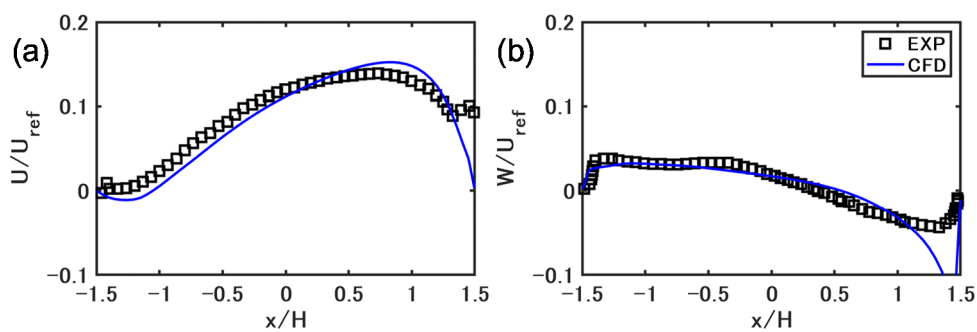
939

940 Fig. S2 Streamwise and vertical direction of mean wind velocities at $z/H = 0.83$.

941

942 Fig. S2 compares the simulated streamwise and vertical direction of mean wind velocities
943 with the experimental values at $z/H = 0.83$. The RNG k–ε model reproduce well the
944 velocities, although the velocities very close to the windward wall show differences with

945 the experimental values. The above validation shows that if suitable inlet conditions are

946 given, the flow field is well reproduced with the turbulence model adopted in this study.